Supplemental material to:

Direct structural identification and quantification of the split-vacancy configuration for implanted Sn in diamond

U. Wahl, J.G. Correia, R. Villarreal, E. Bourgeois, M. Gulka, M. Nesládek, A. Vantomme, and L.M.C. Pereira

Note: numbers of references are with respect to those in the main paper

1. Additional info on Emission Channeling (EC) experimental parameters and data analysis

Both ^{121}Sn ($t_{1/2}$=27.06 h) and ^{121m}Sn ($t_{1/2}$=55 y) were produced at CERN's ISOLDE on-line isotope separator facility [39-40] by means of bombarding a W neutron converter next to a UC_2 target with 1 GeV protons, thus causing neutron-induced fission in the UC_2. Following out-diffusion from the ~2000°C hot target, Sn atoms were selectively ionized to Sn^+ by means of resonant laser ionization [41], followed by 60 kV electrostatic acceleration and high-resolution ($M/\Delta M$~6000) separation of mass 121 using a 90° and 60° magnet. The implanted beam thus consisted of a mixture of ^{121}Sn and ^{121m}Sn. The number of implanted ^{121}Sn+^{121m}Sn atoms was determined as 1.8×10^{10} by integrating the implantation current of ~3pA (corrected for emission of secondary electrons), resulting in the fluence of 2.3×10^{12} cm^{-2} in the beam spot with 1 mm diameter collimation. The β^- activity of the sample was determined from the count rate measured in the pad detector (cf. below) as 56370 Bq. Note that due to the large half-life ratio of ^{121m}Sn and ^{121}Sn (17804:1), the activity of the sample was almost entirely due to the short-lived isotope ^{121}Sn, from which one estimates a number of 7.9×10^9 ^{121}Sn atoms, or 44% of the total number of implanted atoms, the remaining 56% being due to ^{121m}Sn. Note that the ^{121m}Sn activity calculated from this ratio is 4.0 Bq only. The EC measurements in the *as-implanted* state were completed 36.5 h after the implantation, and the sample was then annealed at 920°C in vacuum better than 10^{-5} mbar for 10 min. At this point in time around 27% of the implanted ^{121}Sn+^{121m}Sn atoms had decayed to ^{121}Sb.

The position-sensitive Si pad detector used for the experiments has been described in detail in Ref. [36]. It consists of 22×22 pixels of 1.3×1.3 mm^2 size and was placed at a distance of 301 mm from the sample. As is outlined in Ref. [36], for this geometry the overall angular resolution of the measurements resulting from the size of the detector pixels and the dimension of the 1 mm diameter beam spot on the sample was around 0.1° (standard deviation) for an angular range of ±2.7°.
The total number of events (i.e. particles detected) and resulting average number of events per pixel for each of the measured patterns is given in the following table.

Table S1: Total number of events and average events/pixel for each pattern shown in Figs 2 and 3 of the main paper.

Figure	Channeling axis	Annealing temperature	Total number of events	Average events/pixel
2(a)	<110>	RT	534754	1105
2(b)	<211>	RT	443827	917
2(c)	<100>	RT	745285	1540
2(d)	<111>	RT	703474	1453
3(a)	<110>	920°C	956309	1976
3(b)	<211>	920°C	810015	1676
3(c)	<100>	920°C	896495	1852
3(d)	<111>	920°C	853851	1764

The fit procedures in order to determine the normalization and exact orientation of the patterns, and to identify and quantify the occupied lattice sites were performed as described in Ref. [48] using our proprietary software FDD.
The display of the normalized angular-dependent electron count rate in Figs 2 and 3 of the main paper shows contour plots produced from the 22×22 pixel matrices using the graphical software Origin 8.0. This type of representation is used for display purposes, in the same manner as we have used in all our previous publications for emission channeling patterns measured with a pad detector. It has the advantage of revealing considerably more details to the human eye than simple matrix plots.

2. Implementation of "many-beam" simulations for the diamond structure

In order to quantitatively analyze the experimental electron emission distributions, they were fitted by theoretical emission patterns for various lattice sites, which were calculated using the "many-beam" formalism for electron channeling [33-34, 47]. The many-beam formalism is considered a standard tool in simulating electron diffraction phenomena in periodic structures and finds widespread applications, e.g. in electron microscopy or Reflection High Energy Electron Diffraction (RHEED). Our many-beam implementation for electron channeling simulations closely follows the theoretical work of J.U. Andersen *et al.* [47] on this subject.
Due to the fact that the movement of electrons inside a crystal is subject to diffraction, their trajectories are not well described by the laws of classical mechanics but require a quantum mechanical treatment. Moreover, typical energies of β particles from nuclear decay may reach up

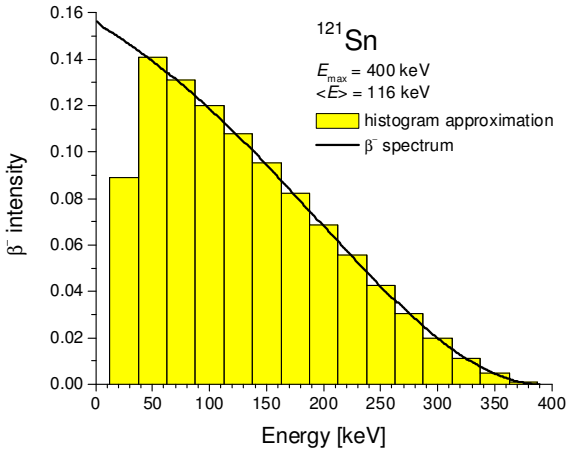

FIG. S1. Histogram of the energy values used to approximate the β^- spectrum of ^{121}Sn in the "many-beam" calculations. Note that the first histogram bar takes into account that the trigger level of the detector was set around 25 keV, hence there was a lower response to detect electrons at this energy.

to several MeV, hence demanding a relativistic description. Both aspects are combined using the many-beam diffraction theory of electron channeling in single crystals. In these calculations, the crystal potential is approximated by a superposition of atomic Doyle-Turner (DT) potentials. The DT potentials result from Hartree-Fock calculations and are parametrized as exponentially screened potentials, in order to make them especially suited for Fourier methods. Since for a description of the channeling effect only electrons moving under relatively small angles with respect to the channeling axis are relevant and these move at relativistic velocities, the potential along the channeling direction can be averaged ("continuum potential") and the electron wave function split into a longitudinal component along the channeling direction, which obeys a relativistic Klein-Gordon equation, and a transverse component perpendicular to the axis, which is given by the solution of a two-dimensional Schrödinger equation in a periodic potential. The β^- particle flux density inside the crystal can then be calculated after obtaining the transverse electron wave function using standard Fourier decomposition and Bloch wave techniques. The many-beam approach has proven to accurately describe EC effects in a multitude of cases, as has been demonstrated and reviewed many times, e.g. in [33-36]. The identification of 10-15% of implanted ^{121}Sn impurities on the BC site in the diamond structure of Ge was demonstrated earlier [37], as was 20-30% on BC sites for ^{59}Fe, ^{67}Cu and ^{111}Ag in Ge [38].

For diamond, the crystal potential was approximated by a superposition of atomic potentials calculated in the Doyle-Turner representation, using the sets of five coefficients a_i and b_i for carbon tabulated in Ref. [44]. To account for the continuous β^- spectrum of ^{121}Sn, many-beam simulations were performed for a number of discrete electron energies (step width of 25 keV in the energy range 25-375 keV and weighted according to the β^- spectrum of ^{121}Sn (Fig. S1). The number of "beams" used in the simulations was 16, which corresponds to $(2\times16+1)^2 = 1089$ Fourier components for the crystal potential and $(16+1)^2 = 289$ for the transverse periodic part of the electron Bloch wave functions. Angular patterns were calculated in x- and y-direction from −3° to +3° in steps of 0.05°. Structural parameters of the diamond used in the calculations were the lattice constant $a = 3.567$ Å and the room temperature (RT) root mean square (rms) displacement of carbon atoms $u_1(\mathrm{C}) = 0.0435$ Å at 293 K, corresponding to a Debye temperature of 1860 K [49]. Assuming that the Debye temperature of ^{121}Sn on C sites scales according to $T_D(^{121}\mathrm{Sn}) = T_D(^{12}\mathrm{C})[12/121]^{1/2} = 586$ K, this leads to an expected value of $u_1(^{121}\mathrm{Sn}) = 0.0337$ Å that is somewhat lower than $u_1(^{12}\mathrm{C})$. While 0.0337 Å was used as default rms impurity displacement in the many-beam calculations for all sites, for the S and BC sites we also calculated theoretical patterns for rms displacements up to 0.5 Å in steps of 0.01 Å.

3. Background correction

Fast electrons moving in matter are subject to pronounced scattering; it is therefore not possible to measure electron emission channeling effects that are not accompanied by a background of scattered electrons. The major contributions are electrons that are backscattered from inside the sample or from the walls of the vacuum chamber. In addition, there exists a background of gammas that are either emitted by the sample itself or originate from natural sources. All types of background contribute to the measured patterns, usually with a rather homogeneous count rate, and thus lower the anisotropy, which means the background increases the random fraction f_R obtained during a fit. In order to correct for this, the non-random fractions f_i need to be multiplied by a correction factor, as is outlined e.g. in Ref. [48]. Note that this procedure is mathematically equivalent to subtracting a flat baseline from the measured patterns.

The contribution of backscattered electrons was estimated by performing GEANT4 [45] Monte Carlo simulations of electron trajectories. GEANT4 is a program package for simulating the scattering and transport of charged particles and finds widespread applications e.g. in the design of particle detectors or for purposes of radiation shielding. Our simulations take into account the main geometrical features and elemental composition of the sample (diamond), the sample holder (Mo), and the vacuum chamber (stainless steel), as well as the energy distribution of β^- particles emitted by ^{121}Sn. According to the simulations, electrons that reach the detector but were initially emitted with a velocity vector pointing away from it (12.9%), as well as electrons that reached the detector after moving inside the walls of the vacuum chamber (29.2%), resulted in an overall background of 36.7% (this percentage is somewhat smaller than the sum of 12.9% + 29.2% = 42.1%

since in the simulations 5.4% of electrons are backscattered both from inside the sample and by the walls), meaning the site fractions f_S and f_{BC} obtained in the fits were multiplied by a correction factor of 1.58.

Background caused by gamma radiation emitted by the radioactive sample, as well as from natural radioactive sources and cosmic radiation, can be experimentally estimated by closing a shutter valve in front of the detector, which stops all electrons from the sample but allows most of the γ particles to pass. This source of background was found to be rather negligible for this experiment since only 0.5-3% of the count rate was contributed by gammas. The reason is that the isotope ^{121}Sn emits no gammas at all and the activity of the diamond sample used (128 kBq at beginning of experiment) provided detector count rates around 60 events/s at the beginning and 10 events/s at the end of the experiment, in comparison to 0.3 events/s from natural background.

The absolute error in performing the background correction as outlined above is estimated at ~±10%. The fact that the sum $f_{sum}=f_S+f_{BC}$ of fitted fractions after background correction reached values above 100% (104% for the analysis of the as-implanted patterns and 112% following 920°C annealing) indicates that the background was overestimated, but still close to the expected range. It should be emphasized that errors in the background correction do of course not at all affect the relative ratio f_{BC} / f_S of BC to *S* site fractions.

4. Considered lattice sites in the diamond structure

Figure S2 shows the (110) plane of the diamond lattice with the positions of the substitutional (*S*) and the major interstitial sites that are obtained by displacing from the S position along <111>, i.e. bond-centered (BC), anti-bonding (AB), tetrahedral (*T*), and hexagonal (*H*); along <100>, i.e. <100>-split (SP) and so-called "Yb" (*Y*, named after Yb) and "C" (*C*, named after its C_{2v} symmetry) sites; and along <110>, i.e. the <110>-split (DS).

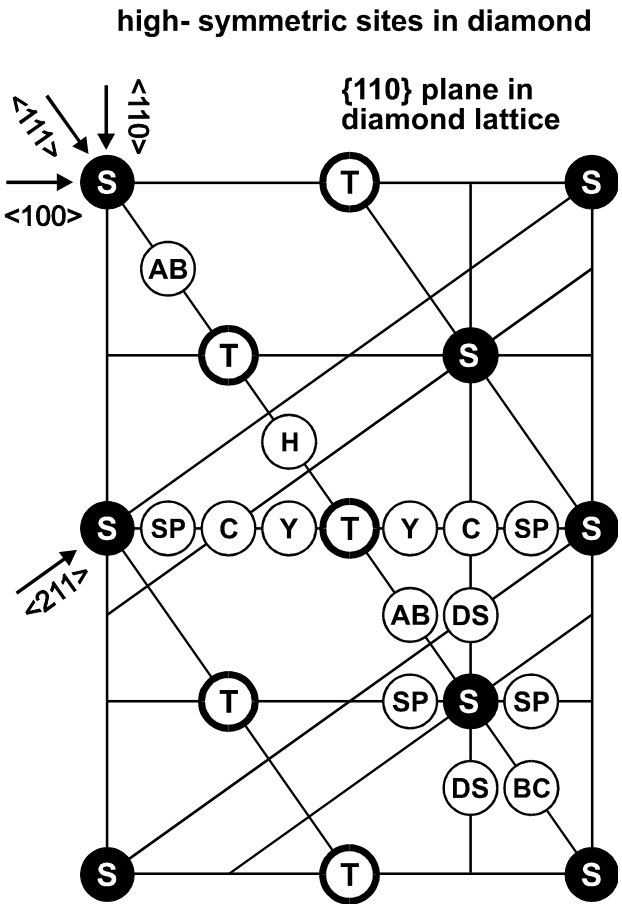

FIG. S2. Positions of the substitutional and major interstitial sites (i.e. those of highest symmetry which are obtained by displacements from substitutional sites along <111>, <100> or <110> directions) in the diamond lattice, shown in the (110) plane.

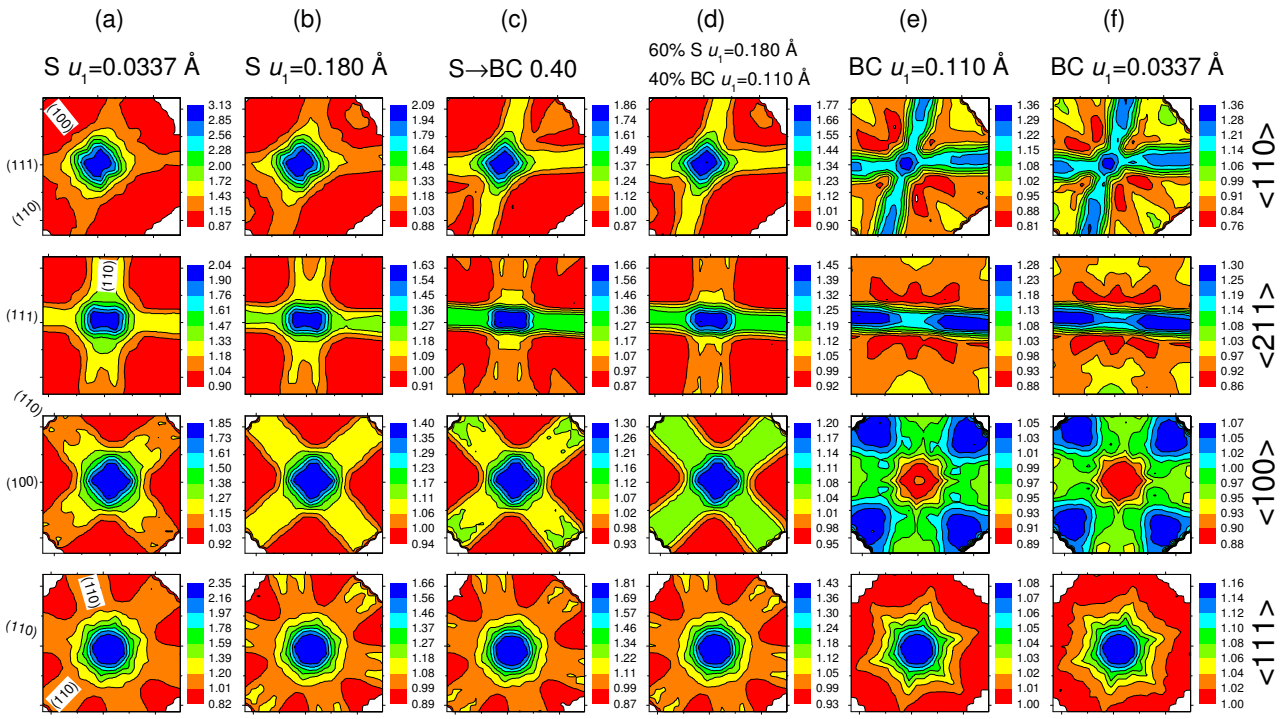

FIG. S3. Theoretical β^- emission patterns around the major crystallographic directions of diamond for ^{121}Sn emitter atoms on the (a) ideal substitutional (*S*) and (f) bond-center (BC) sites, corresponding to the rms displacement $u_1(^{121}\text{Sn}) = 0.0337$ Å. Rows (b) and (e) show emission patterns from *S* and BC sites that are subject to the larger rms displacements of $u_1 = 0.180$ Å and $u_1 = 0.110$ Å, respectively, while row (d) represents a superposition of these two sites with a ratio of *S*:BC = 60:40 (i.e. corresponding to the best fit results in the as-implanted case). Row (c) corresponds to a position that is located at 40% of the distance from *S* to BC sites, i.e. displaced by 0.309 Å from *S* towards BC sites along the <111> direction. All patterns are displayed so as to reflect the orientation of the experimental patterns in Fig. 3 of the main paper, taking into account the angular resolution of the experimental data and the size and orientation of the detector pixels.

5. Theoretical patterns for most relevant lattice sites

<110>, <211>, <100>, and <111> β^- emission patterns from ^{121}Sn were calculated for a total of 245 different positions in the unit cell of the diamond lattice. For the calculations it was assumed that all possible orientations of the sites are populated with equal probability, which assumes that the surface orientation of the sample does not lead to the preferential occupation of certain orientations over others. In Fig. S3 we present those theoretical patterns that turned out to be of particular relevance for the analysis of this experiment. Note that <111> and <100> measurements cannot be used to distinguish between all possible sites: due to the crystal symmetry their channeling patterns for *S* and *T*, or for BC, AB and *H* sites are identical. In order to distinguish unambiguously between these sites it is hence imperative to measure also <110> and <211> directions.

Note that most (but not all) of the features of the angular emission patterns can be understood by means of simple geometrical arguments, taking into account all of the possible equivalent orientations of a lattice site with respect to crystallographic directions, i.e. that the occupation of sites where all possible orientations are aligned with an atomic row or plane will cause channeling effects of emitted electrons along that row or plane, whereas a location for which all projections are interstitial will result in electron "blocking" (rather, enhanced scattering). However, it must be pointed out that this naïve, geometrical approach in terms of channeling/blocking fails completely in case of <110> axial and {111} planar effects resulting from emitter atoms on BC sites. While all four equivalent orientations of BC sites are fully interstitial with respect to all <110> axes and (111) planes, the calculations show that BC sites result in <110> and (111) channeling effects [Figs S3 (e) and (f)]. The reason is that two out of four orientations of BC sites are exactly in the center of close-lying pairs of <110> rows, and three out of four in the center of close-lying (111) planes. Electrons emitted from these locations sense the attractive force of the two neighboring rows or planes as double-well potentials, which keeps them on channeled trajectories.

- Ideal substitutional and bond-center sites characterized by rms displacements of $u_1 = 0.0337$ Å [Figs S3 (a) and (f)] were found for ^{121}Sn atoms following annealing at 920°C. The *S* sites can be clearly distinguished from BC by their <110>, <211> and <100> patterns: in particular <100> axial and (100) planar effects change from channeling for *S* to blocking for BC, thus providing distinct features. However, <111> axial and (110) planar effects only change from strong channeling for *S* to weak channeling for BC, hence <111>patterns are not as well suited to distinguish *S* and BC sites.

- *S* and BC sites with larger rms displacements of $u_1 = 0.180$ Å and $u_1 = 0.110$ Å, respectively [Figs S3 (b) and (e)] are the constituents that, in a ratio of ~60:40 [Fig S3 (d)], provided the best ***two-site*** fit to the data in the RT as-implanted state. Due to the larger rms displacements,

emission patterns from these sites are characterized by an overall reduction in the channeling and blocking anisotropies, which is particular-particularly pronounced for the *S*-site patterns of <110>, <100> and <111> directions, while patterns from BC sites are less affected.
- The site that optimized the ***one-site*** fits for all directions in the as-implanted state corresponds to a position that is displaced from *S* sites along <111> by ~40% of the distance towards BC sites, i.e. by 0.32 Å [Fig. S3 (c)]. Note that the <110> and <211> patterns for that position are very similar to the ones shown in column (d) for the 60:40 ratio of *S* and BC sites with larger rms values. Correspondingly, the chi square of fit was only slightly better for the *two-site* fit in these cases (2.3% and 0.4% improvements). However, <100> patterns in columns (c) and (d) show a more pronounced difference, and in this case option (d) provided a 5% improvement in chi square of fit.

6. Particularity of <111> patterns

The improvements in the chi square of fit when introducing a second site in addition to *S* sites were rather small for the <111> patterns, at maximum 3.5% for the as-implanted and 1.5% for the 900°C annealed measurement, thus providing only a small margin for identifying the best results from the patterns of this direction. The reason for the comparatively small changes in chi square are that <111> patterns from *S* and BC sites [cf. Fig. S3 (a) and (f)], although *quantitatively* characterized by quite different maximum yields (2.35 for *S* sites *vs* 1.16 for BC sites), are *qualitatively* still similar: the <111> direction shows channeling effects. The particular reason for this is that when measuring any <111> direction, ¼ of emitter atoms in BC positions are perfectly aligned with this direction, while ¾ are interstitial to it. Since for electrons the channeling effects from aligned probe atoms are much stronger than "blocking" effects from interstitial ones, they still dominate the overall effects from BC sites.
The patterns measured for the <111> orientation of this sample suffered from a slightly inhomogeneous (in the % range) background, where the count rate in the lower part of the patterns is somewhat higher than in the upper part, as can be seen from Figs 2 (d) and 3 (d) of the main paper. This was caused by the fact that the 3 mm sized diamond sample had to be mounted in such a way that the beam spot was located relatively close to one of the clamps that hold the sample (which is hard to avoid for a beam spot of 1 mm on such a small sample). Due to the unusual surface orientation of the sample (surface 8° off from a <110> direction), in order to reach a <111> direction the sample holder had to be azimuthally rotated by 130° compared to the other measurements, which put this clamp close to the path of the electrons towards the detector. The inhomogeneous background was then caused by the contribution of electrons that do not reach the detector on a direct path but are scattered in the clamp. Unfortunately this inhomogeneous background had the effect to make the results of the two-site fits with S and BC sites unstable, since the fitting routine tried to adjust the fractions so as to better match the inhomogeneities of the background. We therefore had to exclude the <111> results from the two-site analysis. The theoretical patterns included for the <111> direction in Figs 2 (h) and 3 (h) of the main paper are hence not for the best fit results of that direction, but when the relative contribution from BC sites was fixed at the ratios that were derived from the analysis of the other three directions, i.e. $f(S) : f(\mathrm{BC}) = 60:40$ at RT as-implanted, and at 70:30 for 920°C annealed. As can be seen, Figs. 2 (h) and 3 (h) match the experimental results of Figs 2 (d) and 3 (d) quite well; the <111> measurements are therefore compatible with the results from the other directions.

7. Chi square analysis of possible ^{121}Sn displacements

7.1 One-site fits

All patterns were first analyzed by allowing only one lattice site, besides "random" sites, in the fits. Note that the contribution from so-called random sites corresponds to a flat pattern without anisotropies. Such a contribution always needs to be allowed when fitting emission channeling patterns. It includes effects from emitter atoms that could be located for instance in heavily damaged regions of the sample, where no channeling effects are possible, or emitter atoms on lattice sites of such low crystal symmetry that emitted β^- particles are subject to negligible channeling effects, but also any effects from a homogeneous background of scattered electrons or from gammas are included in the random fraction. Effects from background are later corrected by multiplying the fitted site fractions with a correction factor (cf. Section 3.), which at the same time reduces the random fraction.

For one-site fits, when only considering major highly symmetric sites such as *S*, BC, AB, *T*, *H*, SP, *C*, *Y*, and DS, clearly the substitutional position provided the best fit for all patterns; however, the best results with lowest chi square were not obtained for ideal substitutional sites but for positions that are displaced from the substitutional sites along <111> directions (Fig. S4). In the as-implanted state, displacements of 30-50% of the distance from *S* to BC sites, i.e. 0.23-0.39 Å, improved chi square by 4% for <111>, 14% for <100>, 37% for <211>, and 44% for <110>. In the 920°C annealed state displacements of 10-30% of the distance from *S* to BC sites, i.e. 0.08-0.23 Å, improved chi square by 3% for <111>, 4% for <100>, 9% for <211>, and 19% for <110>.

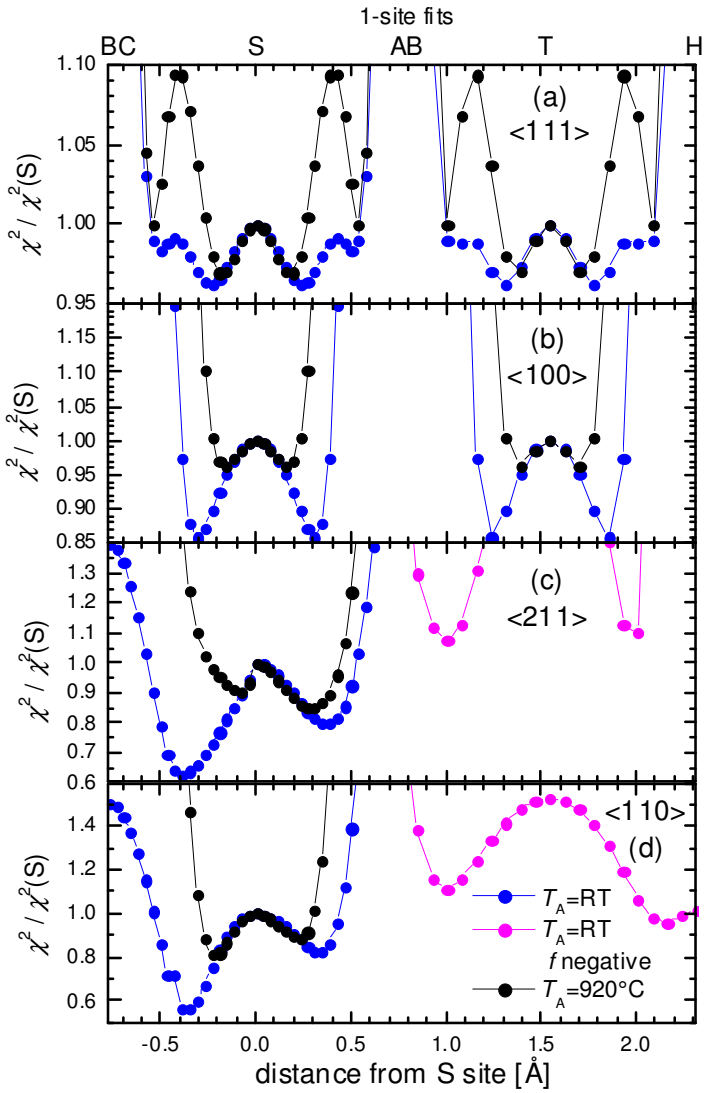

FIG. S4. Relative chi square of ***one-site*** fits as a function of the position along the <111> direction, normalized by dividing by the chi square resulting from *S* sites. Note that <111> and <100> results cannot be used to distinguish between all possible sites since due to the crystal symmetry their channeling patterns for *S* and *T* or BC, AB and *H* sites are equal. The plots have been scaled so as to provide good resolution near the minima of the chi square and therefore values that fall above the chosen chi square range are not shown. The parts of the curves shown in magenta color correspond to fits with a negative site fraction, hence physically irrelevant results.

7.2 Two-site fits with S site kept fixed

For two-site fits, initially the first site was kept fixed at the ideal substitutional position, while the position of the second site was allowed to vary within the range of all calculated patterns. It is obvious that the chi square of such two site fits will always be better than the chi square of the one-site fit for the position that is kept fixed, which is therefore used for comparison [Fig. S5].

In the 920°C annealed state, this analysis led to ideal BC sites being the second site that provided the best fits, with chi square improvements of 7% for <100>, 19% for <211>, 24% for <110> compared to *S*-site fits only [Fig. S5].

In the RT as-implanted state, when the S site was kept fixed, improvements in chi square of 5% for <100>, 38% for <211> and 45% for <110> were achieved, however, not at ideal BC sites but at positions located about 0.2-0.4 Å on the way to *S* sites, which is a clear indication that some displacement from BC sites plays a role in this case.

Note that when performing two-site fits it is under certain circumstances a common phenomenon that negative fractions may be obtained for one of the sites. Such fit results with a negative fraction are indicated in Fig. S5. This phenomenon is particularly often observed when the two sites that are used in the fit are lying close together, which leads to patterns that are not much different from each other, e.g. if fitting an ideal *S* site plus a second site that is located rather close to it, as is the case for the red and magenta parts of the curves in Fig. S5. In this case the fit procedure optimizes the fractions on small differences in the two patterns, with the results that one fraction becomes negative and the other too highly positive, with only the positive sum of both being in a physically relevant range. As is described in section 5, this phenomenon occured for two-site fits of <111> patterns, so that these could not be used for an optimized two-site analysis. However, the <100>, <211> and <110> patterns of *S* and BC sites are substantially different, cf. Fig. S3, and statistically relevant improvements of chi square were associated with entirely positive site fractions that were very similar for each of the three directions, which gives additional confidence in the results.

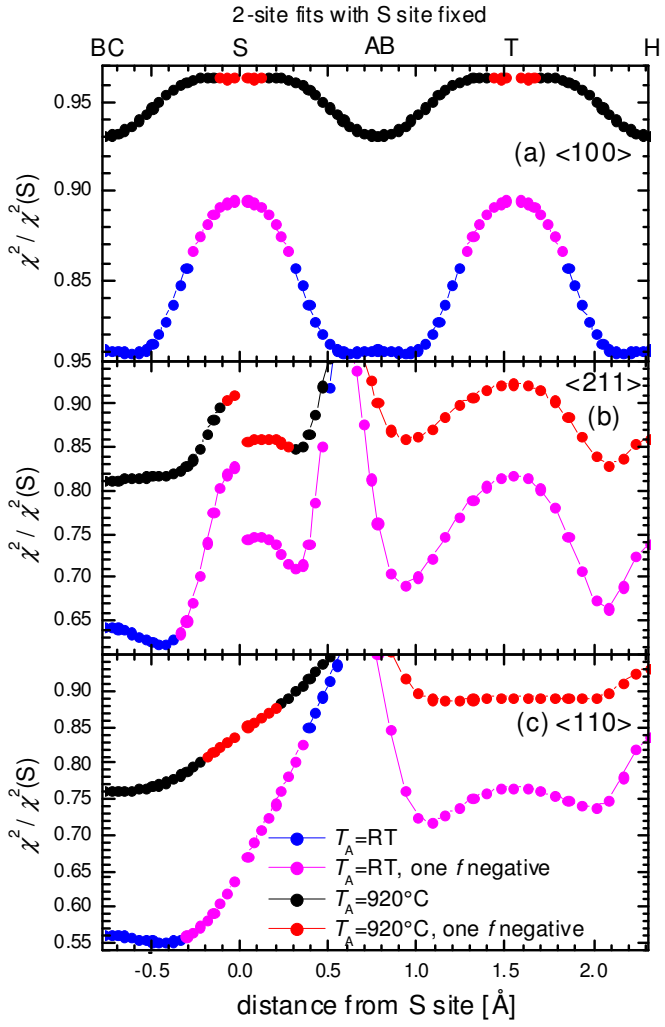

FIG. S5. Relative chi square of ***two-site*** fits as a function of the position of the second site along the <111> direction while keeping the first site fixed at the S position, normalized by dividing by the chi square resulting from S sites only. The parts of the curves shown in red or magenta colors correspond to fits with one negative site fraction, hence physically irrelevant results.

7.3 Two-site fits with BC site kept fixed

When two-site fits were performed where the first position was kept fixed at ideal BC sites, in the 920°C annealed case the ideal *S* sites provided the lowest chi square as position for the second site (Fig. S6). The associated large improvements in chi square of 85-90% are due to the fact that without including *S* sites no good fits of the experimental patterns are possible.

However, in the RT as-implanted case the positions of the second site that optimized the chi square were not ideal *S* sites but displaced by 0.2-0.4 Å from the *S* sites, with displacements from *S* to BC or AB sites giving quite similar results. This is a strong indication that in the as-implanted state also the *S* sites involved are not ideal. Moreover, one may conclude that it is not possible to reliably identify, at the same time, which static displacements from both *S* and BC sites provide best fits. Hence, we adopted the approach to model the experimental data by Gaussian spreads of displacements from the ideal *S* and BC sites, as is described in the following section.

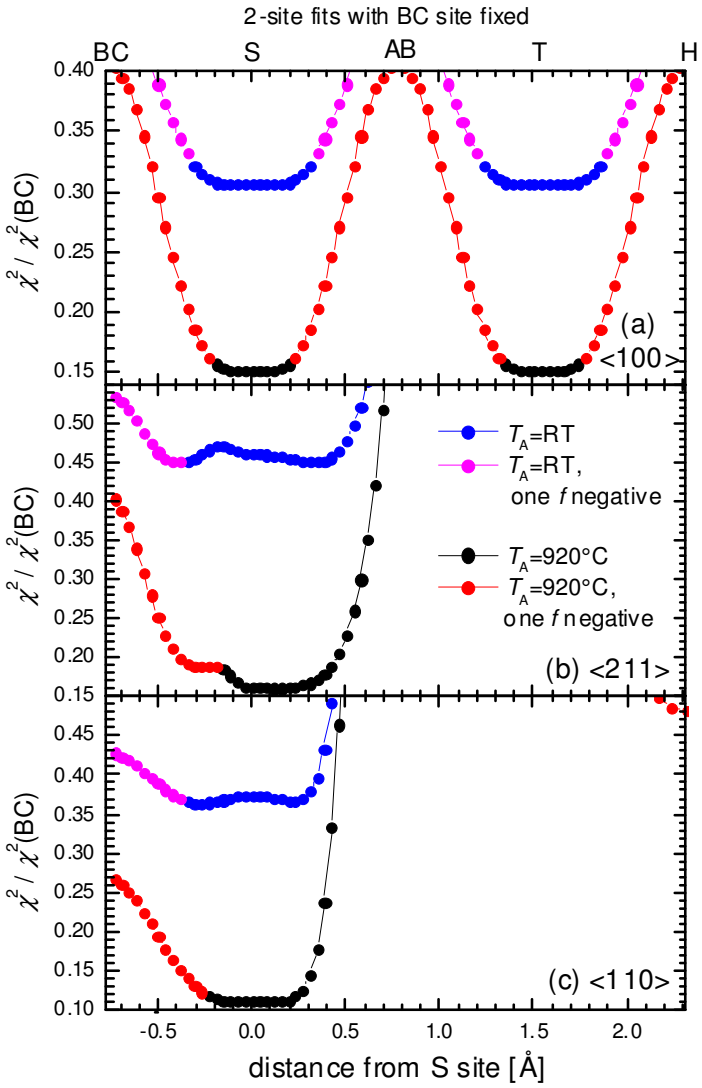

FIG. S6. Relative chi square of ***two-site*** fits as a function of the position of the second site along the <111> direction while keeping the first site fixed at the BC position, normalized by dividing by the chi square resulting from BC sites only. The parts of the curves shown in red or magenta colors correspond to fits with one negative site fraction, hence physically not relevant results.

7.4 Two-site fits with varying rms displacements from S and BC positions

As was mentioned in the previous section, fits were performed whereby the rms displacements from *S* and BC sites were varied for all possible combinations of $u_1(S)$ and u_1(BC) in the range from 0.01 Å to 0.30 Å in steps of 0.01 Å. The resulting chi square values are shown as matrix plots with contours in Figs S7 and S8.

7.4.1 RT as-implanted state: As can be seen from Figs S7 (a)-(c), there is a clear trend that for both sites rms displacements that are considerably larger than expected from thermal vibrations are minimizing the chi squares. However, since there is some spread in the combinations of $u_1(S)$ and u_1(BC) that provided the best fits for the three measured directions, as a compromise to find an overall good fit using the same sites for all three cases, we have plotted in Fig. S7 (d) the sum of the chi squares from the fits of the three directions, which shows a minimum for $u_1(S)$ = 0.18 Å and u_1(BC) = 0.11 Å.

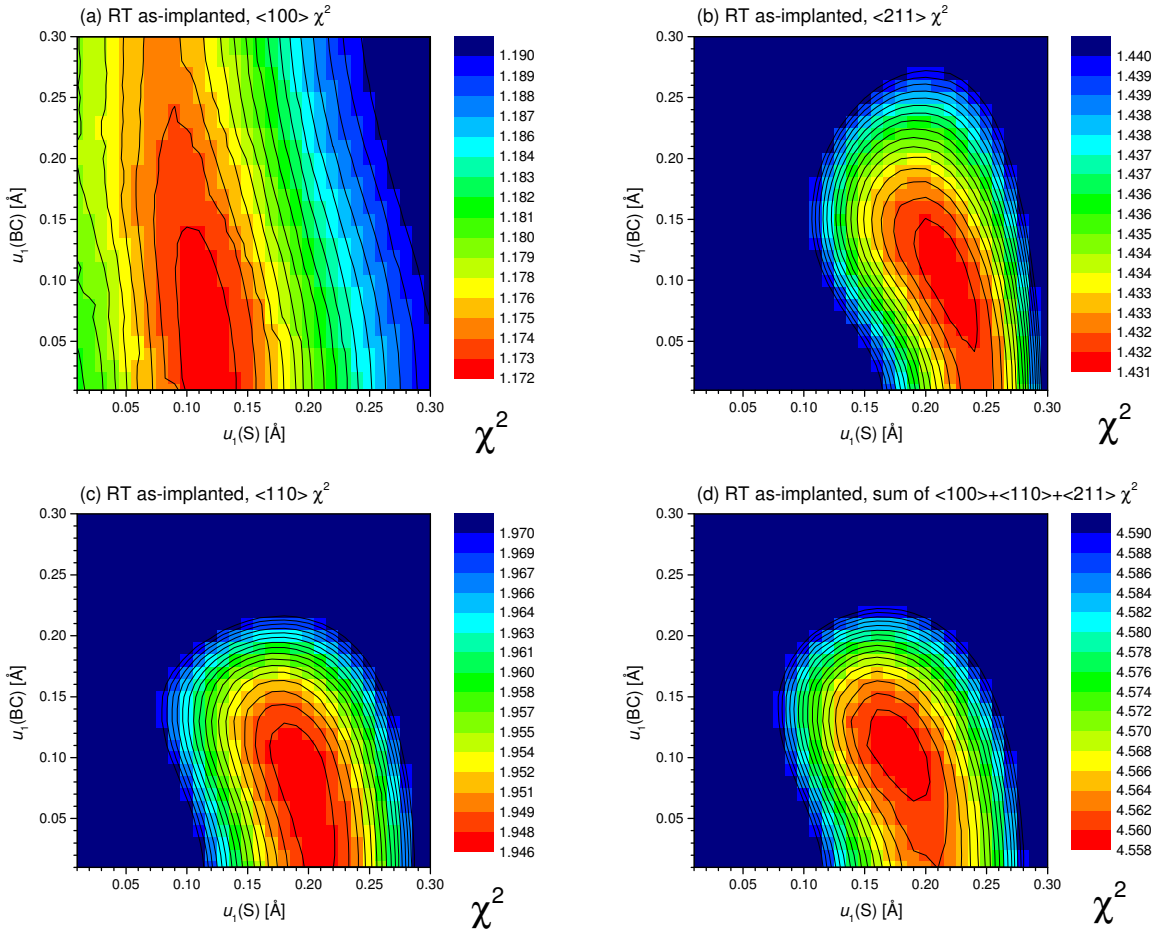

FIG. S7. Matrix plots with contours of the reduced chi square of ***two-site*** fits with *S* and BC sites as a function of the rms displacements $u_1(^{121}\text{Sn})$ from *S* and BC positions in the RT as-implanted state . Panel (a) is for <100> fits, (b) for <211> fits and (c) for <110> fits, while (d) represents the sum of the chi squares from the fits of all three directions. The dark blue regions represent chi square values that are above the limits shown by the color bars.

7.4.2 920°C annealed state: Figs S8(a)-(c) show the matrix plots for the obtained chi squares when the rms displacements from *S* and BC sites were varied for all possible combinations of $u_1(S)$ and u_1(BC) in the 920°C annealed state. In this case the rms displacements that provided the best fits were in most cases quite close to the ones expected from thermal vibrations, with only the <211>results indicating a somewhat higher value for $u_1(S)$.

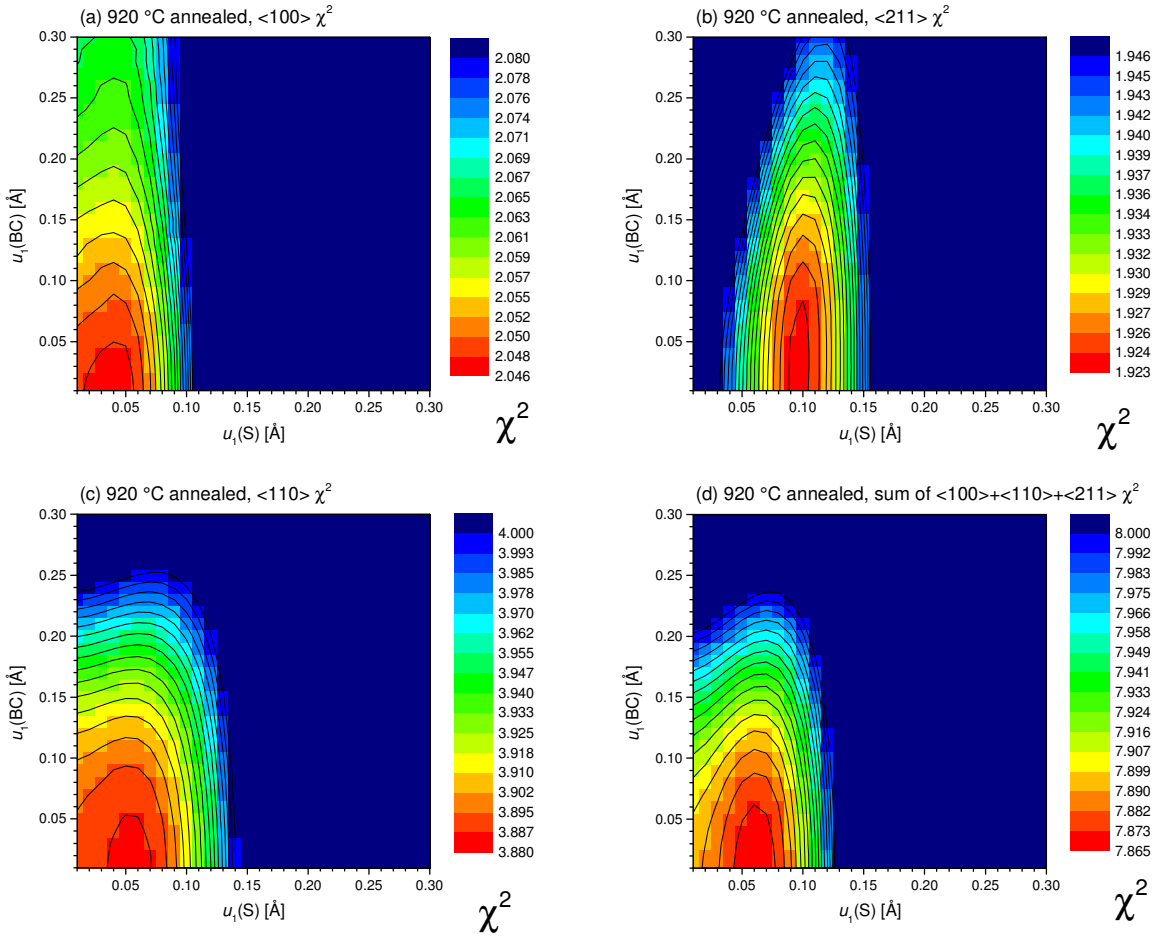

FIG. S8. Matrix plots with contours of the reduced chi square of ***two-site*** fits with *S* and BC sites a function of the rms displacements $u_1(^{121}\text{Sn})$ from *S* and BC positions following annealing at 920°C. Panel (a) is for <100> fits, (b) for <211> fits and (c) for <110> fits, while (d) represents the sum of the chi squares from the fits of all there directions. The dark blue regions represent chi square values that are above the limits shown by the color bars.

8. Possible influence of changes in the Sn depth profile on the analysis

As mentioned in Ref. [48], approximations related to dechanneling and insufficient knowledge of the probe atom depth profile are possible sources of uncertainty which may limit the quantitative analysis of electron channeling patterns.

Dechanneling of electrons is caused by two basic processes, and the relative importance of both varies with the type of crystal where the channeling effect takes place, with temperature, and also with the electron energy. On the one hand, the channeling electrons scatter with other electrons in the crystal. The inverse of the mean free path length λ_{pl} for electron-electron scattering with large momentum transfers in a free electron gas is given by [47]

$$\lambda_{pl}^{-1} = \frac{1}{2}\frac{e^2\omega_p}{\hbar v^2}\ln\frac{4m_e v^2}{\hbar\omega_p}$$

where e is the electron charge, m_e its rest mass, v its relativistic velocity, and ω_p the plasmon frequency, which is being estimated for diamond to be 4.74×10^{16} Hz (corresponding to 31.2 eV) assuming a free electron gas of 4 valence electrons/atom. Electronic scattering thus causes an exponential depopulation of channeling electrons, which depends on the electron energy as shown in Fig. S9.

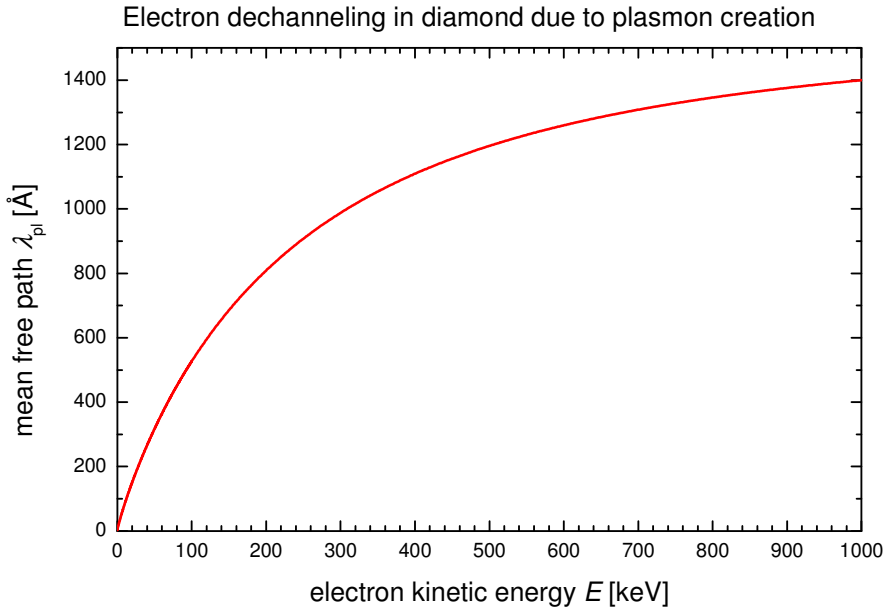

FIG. S9. Mean free path length λ_{pl} (often also called "coherence length") for dechanneling in diamond due to the creation of plasmons. For β^- particles from ^{121}Sn with a maximum energy of 400 keV, the exponential depopulation means that channeling effects entirely disappear after a few thousand Å.

On the other hand, dechanneling is also caused through scattering of the channeled electrons by the thermally vibrating atoms of the crystal. Our implementation of this source of dechanneling also follows the description of Ref. [47], i.e. scattering of the Bloch waves is treated in quantum-mechanical 1st order perturbation theory (Born approximation). This type of scattering strongly depends on the nuclear charge Z and thermal vibration amplitude u_1 of the crystal host atoms, so that it forms the dominant source of dechanneling in high-Z materials with large vibration amplitudes as, e.g., Ge, while in diamond it only contributes with mean free path lengths that are longer than the scattering by the creation of plasmons; the latter is particularly pronounced in diamond due to its high atomic density and related high plasmon frequency.

Dechanneling thus causes a complete breakdown of the channeling effect on a length scale which for diamond lies in the region of a few thousand Å. It also means that the use of an incorrect depth profile in the simulations, i.e. too deep, too shallow, or too wide, would result in a change of the site fractions derived by the fitting procedure. We have estimated possible influence of this effect by analyzing our experimental data not only with the ^{121}Sn depth profile of 210(40) Å expected from SRIM [42], but also with a number of other profiles (Table S2).

Table S2: Fit results for the background-corrected site fractions f_S and f_{BC} in the 920°C annealed state when using S and BC site patterns calculated for emitter atoms that are subject to different Gaussian depth profiles of projected range R_p and straggling ΔR_p. The chi square of fit χ^2 is given in each of the cases. The values shown in red correspond to the ^{121}Sn depth profile calculated by SRIM [42] for 60 keV implantation and are the ones used in the actual analysis. Note that R_p is somewhat different for each crystallographic axis since the path length of electrons out of the crystal varies with respect to the angle of the axis towards the surface normal of the sample.

Axis	Angle to surface normal	R_p [Å]	ΔR_p [Å]	f_S [%]	f_{BC} [%]	f_{sum} [%]	f_{BC}/f_S	χ^2 of fit
<110>	8°	116	18	49.3	22.9	72.2	0.465	5.01
		149	38	58.1	27.7	85.8	0.477	3.90
		211	**40**	**68.3**	**35.7**	**104.0**	**0.523**	**3.89**
		300	81	88.3	50.6	138.9	0.573	3.69
		417	99	112.8	77.9	190.7	0.691	3.99
		547	140	143.3	98.3	241.6	0.686	3.95
<211>	22°	116	18	56.2	11.9	68.1	0.212	2.44
		149	38	63.7	19.8	83.5	0.311	2.16
		218	**47**	**79.0**	**33.8**	**112.8**	**0.428**	**2.09**
		300	81	94.3	45.2	139.5	0.479	2.02
		417	99	119.8	59.4	179.2	0.496	2.00
		547	140	150.2	67.3	217.5	0.448	2.01
<100>	51°	116	18	51.2	30.8	82.0	0.602	2.30
		149	38	56.1	31.4	87.5	0.560	2.22
		193	36	63.0	32.2	95.2	0.511	2.20
		274	**53**	**76.8**	**35.7**	**112.5**	**0.465**	**2.05**
		417	99	101.1	46.1	147.2	0.456	1.95
		547	140	123.6	55.8	179.4	0.451	2.00

The fact that the derived sum fractions lie for all three axes close to 100% and show a relatively small spread gives confidence that a) the depth profile estimated by SRIM corresponds to the actual depth profile of the implantation, b) that the dechanneling approximations work well, and c) that the background correction as described above in section 3 is also within the expected precision range of 10%, hence that the overall analysis of sum fractions is sound. Moreover, since the derived sum fractions before and after the 920°C annealing are quite similar, one may conclude that the ^{121}Sn profile did not significantly shift during the annealing step.

9. Experimental details of confocal PL measurements

Following the radioactive decay of short-lived ^{121}Sn to ^{121}Sb, the photoluminescence (PL) properties of the sample containing still the long-lived ^{121m}Sn were studied using a home-built confocal PL microscope at the Institute for Materials Research, Hasselt University [46]. Green excitation light (532 nm, laser power of 1 mW) was focused onto the sample using an objective with numerical aperture of 0.95, thus giving a depth resolution of ~4 µm. The photoluminescence spectra were analysed using a Shamrock 193 imaging spectrograph equipped with an EM-CCD ANDOR camera (used spectral resolution 0.2 nm) and an Excelitas Si APD single photon counter. Depth-dependent PL measurements were performed at room temperature (Fig. 4 of the main paper) and comparable results measured in several different spots by scanning the laser within a range of ~100 µm over the sample (Fig. S10). In Fig. 4 of the main paper, PL signals from SnV^- are visible with decreasing intensity as a function of depth below the surface. However, the fact that they are at all visible at depth windows deeper than "at surface level" is due to the limited depth resolution (~4 µm) of the confocal PL technique with the specific objective lens used in the measurements, so that signals from SnV^- only disappear from the PL spectrum once the focus of the confocal microscope is set to a depth of 11 µm. The absence of ^{121}Sn diffusion during annealing can be concluded as was described in the previous section, so this can also be assumed to be the case for ^{121m}Sn. Impurity diffusion in diamond is extremely slow, and there is no indication in the literature that an element of similar chemical nature and atomic size as Sn should diffuse during relatively mild annealing at 920°C. In fact, in Refs [15] and [21] Sn implanted samples were treated at temperatures up to 2100°C without any effects of diffusion being reported from the outcome of confocal PL microscopy.

10. Distribution of SnV^- ZPL emission in the sample

Series of confocal 100×100 µm^2 integral PL maps (using a cut-off filter at 650 nm for the detection, so the light with shorter wavelengths is suppressed) were performed for two areas of the sample, about 0.3 mm apart from each other (Fig. S10). For several spots within these maps the focus depth was changed, and full PL spectra measured. It turns out that the PL intensity integrated >650 nm is quite inhomogeneously distributed. Further spectral imaging shows that in the areas with a large PL intensity the signals from N*V* centers are prominent in the spectra. In contrast, the 621 nm ZPL from SnV^- is only observed in spots where the integral PL intensity is low and N*V* signals marginal or absent. In particular, in the areas of high PL, the map counts are about 10–20 times higher than in the spots with observed Sn*V* luminescence. The N*V* background in these areas can therefore mask the Sn*V* PL. Concerning the inhomogeneity of N*V* distribution, natural type IIa diamond contains N in the concentration <1 ppm which is inhomogeneously distributed, some N existing already in the form of N*V*. Further N*V*s may be generated in the implanted depth region due to the vacancies resulting from Sn implantation (in the peak of the damage cascade the initial vacancy concentrations exceed 1 ppm by more than a factor of 2000). Since natural IIa diamond can also contain locally some other impurities, those might lead to a different charge environment and N*V* PL spectral quenching.

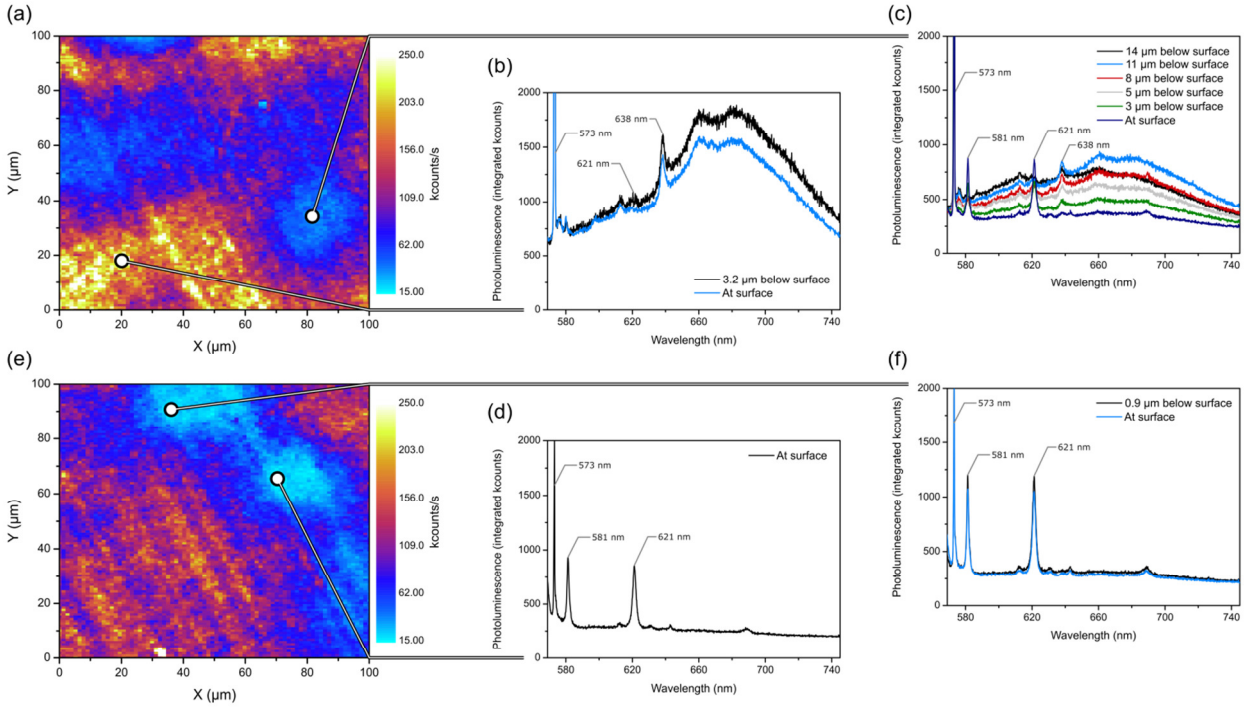

FIG. S10. Confocal 100×100 µm^2 maps of the integral PL intensity >650 nm for area 1 **(a)** and area 2 **(e)** of the sample. **(b)** PL spectra focusing on two different depths at a spot in area 1 which was chosen within a region of high integral PL intensity. The spectra are dominated by the ZPL of NV^- at 638 nm and its phonon sidebands at higher wavelengths. **(c)** PL spectra focusing on various different depths at a spot in area 1 which was chosen within a region of low integral PL intensity. These are the spectra which are shown in Fig. 4 of the main paper. **(d)** and **(f)** show near-surface PL spectra from two spots in area 2 within regions of low integral PL intensity. In all three cases (c), (d) and (f) the sharp ZPL of SnV^- at 621 nm and the 582 nm line of unknown origin are clearly visible.

11. Linewidth of 621 nm SnV^- ZPL

Since the SnV^- ZPL was subject to an almost flat background, it could be directly fitted by a Lorentzian as shown in Fig. S11.
In Table S3 we have compiled the room temperature linewidths of SnV^- centers under 532 nm excitation found in the literature.

Table S3: Sample type, implantation (or growth) parameters, sample annealing procedure and RT linewidths of the SnV^- 621 nm emission line in diamond single crystals from the literature.

Reference	Sample type	Implanted fluence [atoms/cm^2] or growth method	Implantation energy	Annealing temperature, time and atmosphere	RT FWHM linewidth [nm]	Ensemble or single center
[12] Tchernij *et al* 2017	"electronic grade" from ElementSix	5×10^{13}	10 MeV	950°C, 2 h, vacuum	7	ensemble
[13] [2] Iwasaki *et al* 2017	"electronic grade" type IIa from ElementSix	2×10^{13}	130-150 keV	800°C, 30 min, vacuum 800°C, 30 min, 7.7 GPa 1200°C, 30 min, vacuum 1200°C, 30 min, 7.7 GPa 1500°C, 30 min, vacuum 1500°C, 30 min, 7.7 GPa 2100°C, 30 min, 7.7 GPa	12 11.3 8.3 9.7 7.6 7.2 6.2	ensemble
		2×10^{8}	150 keV	2100°C, 30 min, 7.7 GPa	6	single center
[14] Alkahtani *et al* 2018	"ultra pure" from ElementSix	1×10^{12}	not specified	800°C + 1500°C, "several hours", vacuum	4.2	ensemble
[20] [2] Görlitz *et al* 2019	"electronic grade bulk diamond"	2×10^{13}	700 keV	2100°C, 30 min?, 7.7 GPa	~6.7 [2] 6.15	ensemble single center
	"electronic grade bulk diamond"	"varying doses"	80 keV	1200°C, 4 h	1.98	single center
This work 2019	natural type IIa	2×10^{12}	60 keV	920°C, 10 min, vacuum	2.3	ensemble
[15] [3] Ekimov *et al* 2018	high-pressure high-temperature grown	Sn incorporated during growth from $Sn(C_6H_5)_4$ precursor		growth at 1430-1730°C, 8-9 GPa	6-7	ensemble
[16] [3] Palyanov *et al* 2019	high-pressure high-temperature grown	Sn incorporated during growth via TGG method		growth at 1700-1900°C, 6.3-7.5 GPa	0.3 @ 80 K	ensemble

[1] linewidths from Ref. [13] were extracted from the Fig. 1 of this Ref.
[2] "C"-line width extracted from Fig. 6 of this Ref.
[3] Ref [16] only reports FWHM linewidths measured at 80 K.

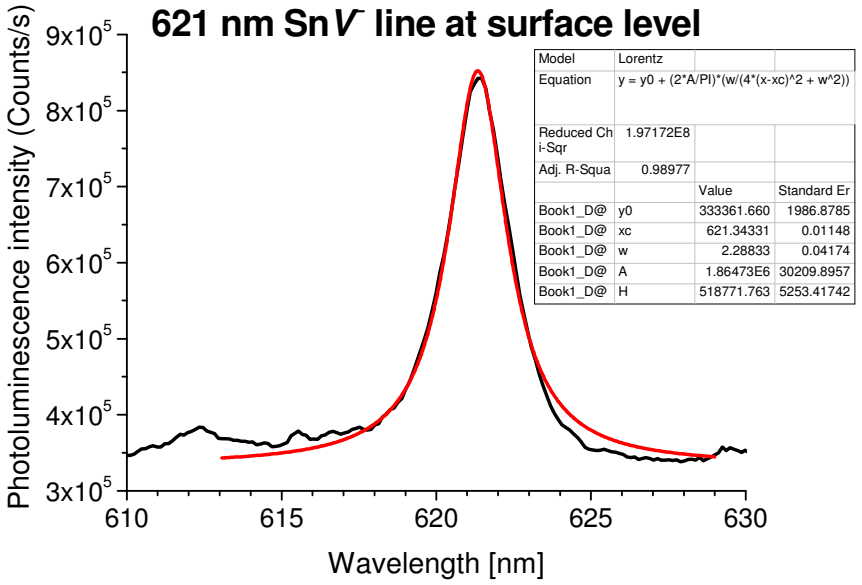

FIG. S11. Magnification of the region around the 621 nm ZPL of SnV^- (black) with a Lorentzian fit of FWHM 2.3 nm (red). Note the line shape is very near ideal Lorentzian, indicating a very narrow distribution of single center emission lines in the whole ensemble.

12. Linewidth of the 582 nm emission line and its possible sources

As mentioned in the main paper, this line was found at exactly the same position (581.4 nm) and with a FWHM of 1.5 nm (Fig. S12) as what has been termed the "L1 center" by John *et al* [50] and Lühmann *et al* [32] at 581.7 nm with FWHM <1.4 nm. In our sample, its depth-dependent intensity is confined to the near-surface region, as is the one of SnV^- (Table S4), which points towards it being related to the ^{121}Sn+^{121m}Sn implantation.

Table S4: Depth dependent intensity and FWHM of the 621 nm and 582 nm lines.

Focus depth [µm]	Integral 621 nm line	FWHM 621 [nm]	Integral 582 nm line	FWHM 582 [nm]	Ratio 582/621
0	1864730	2.29	1284160	1.53	0.6887
2	980383	2.43	724870	1.71	0.7394
5	694587	3.04	344196	1.47	0.4955
11	440026	4.5	100355	1.70	0.2281

John *et al*. found the L1 center in "electronic grade" CVD diamond that was implanted at mass 27 with a possible mix of several molecular, negative ions for which they suggested ^{13}C^{14}N, ^{12}C^{15}N or ^{11}B^{16}O. The conditions for observing the center were hence totally different from ours. Several scenarios may be considered:

a) Contribution of the stable decay product ^{121}Sb:
While Sb is not ionized by the type of laser ion source used to produce the ^{121}Sn+^{121m}Sn beam at ISOLDE, it builds up over time in the sample as a result of both the decay of ^{121}Sn and ^{121m}Sn. At the time of the PL measurement, with ^{121}Sn having completely decayed into ^{121}Sb, this isotope should hence have been present in the sample at roughly the same amount as ^{121m}Sn, and with a depth profile that corresponds to the one of Sn (unless Sb should have diffused during sample annealing).

b) Contaminations of the mass 121 beam:
Due to the high mass resolution of the ISOLDE HRS isotope separator used ($M/\Delta M$~6000), contaminations by ions of the neighboring masses 120 and 122 can be ruled out. While surface-ionized molecular ions such as oxides or fluorides are a possibility, at mass 121 this would need to be ions like ^{105}Pd^{16}O, or ^{103}Rh^{18}F, which seems quite unlikely, or perhaps ^{87}Sr^{34}S. Doubly charged molecular ions of mass 242 are even less likely.

Summarizing a) and b), from our sample preparation conditions, an Sb-related defect would be a prime candidate for the 581.5 nm line. However, this does not match the scenario of L1 being produced by implantations of mass 27 molecules, as described in Refs. [32, 50]. In any case, it would be highly surprising having created such a bright center, which is similar in intensity to the SnV^- ZPL, from a contamination of our ^{121}Sn+^{121m}Sn beam.

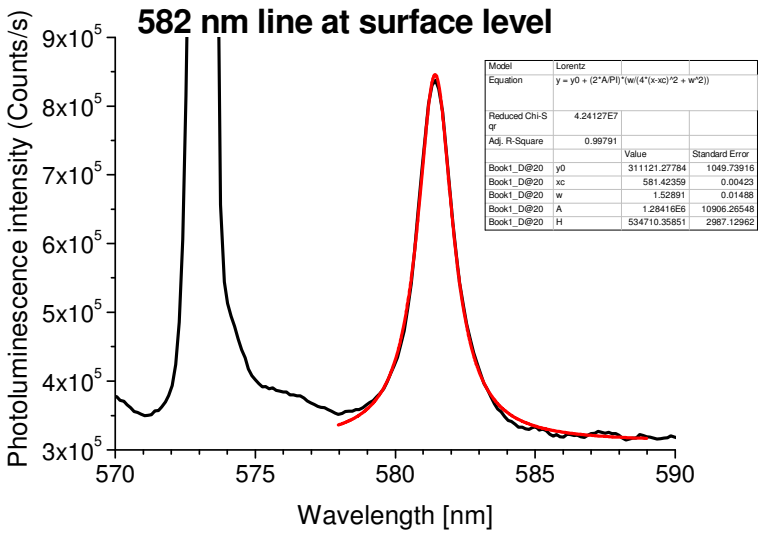

FIG. S12. Magnification of the region around the 582 nm possible L1 line (black) with a Lorentzian fit of FWHM 1.5 nm (red). Note the almost perfect Lorentzian line shape.

c) The center is due to a native defect created by ion implantation and can thus be produced by various types of ions. Implantation defects have a shallower depth profile, peaking somewhat closer to the surface than the projected range of the implant. With the limited depth resolution of confocal PL, the line would then show quite the same response to changing the focus depth as the 620 nm SnV^- line (which was the case). This scenario, however, cannot explain why the 582 nm line was not observed following the ^{120}Sn implantations of Refs. [12-14, 17-19], or reported in the literature following implantation of a variety of other ions like N, P, B, Si, Ge, Pb, Mg, Ca etc.

d) The center is due to an unknown grown-in impurity near the surface of the natural diamond that we used (note that the line was not observed in the bulk of the diamond and its intensity shows a similar depth dependence as the one of SnV^-). This scenario cannot be excluded, however, given the amount of studies performed on the luminescence of natural diamonds and the available literature on the subject, it seems unlikely that such a bright defect should have escaped notice.

We conclude that none of the presented scenarios is currently offering an entirely satisfying hypothesis concerning the nature of the 582 nm line.

13. PL results of stable ^{120}Sn implantation

In an attempt to reproduce the same conditions as for the previous radioactive experiment, the backside of the same sample was subsequently implanted with stable ^{120}Sn at 60 keV, aiming at a fluence of 2×10^{12} atoms/cm^2 and using the ion implanter at the laboratory of Quantum Solid-State Physics in Leuven. However, due to technical limitations of the implanter at that time, we do not consider the targeted

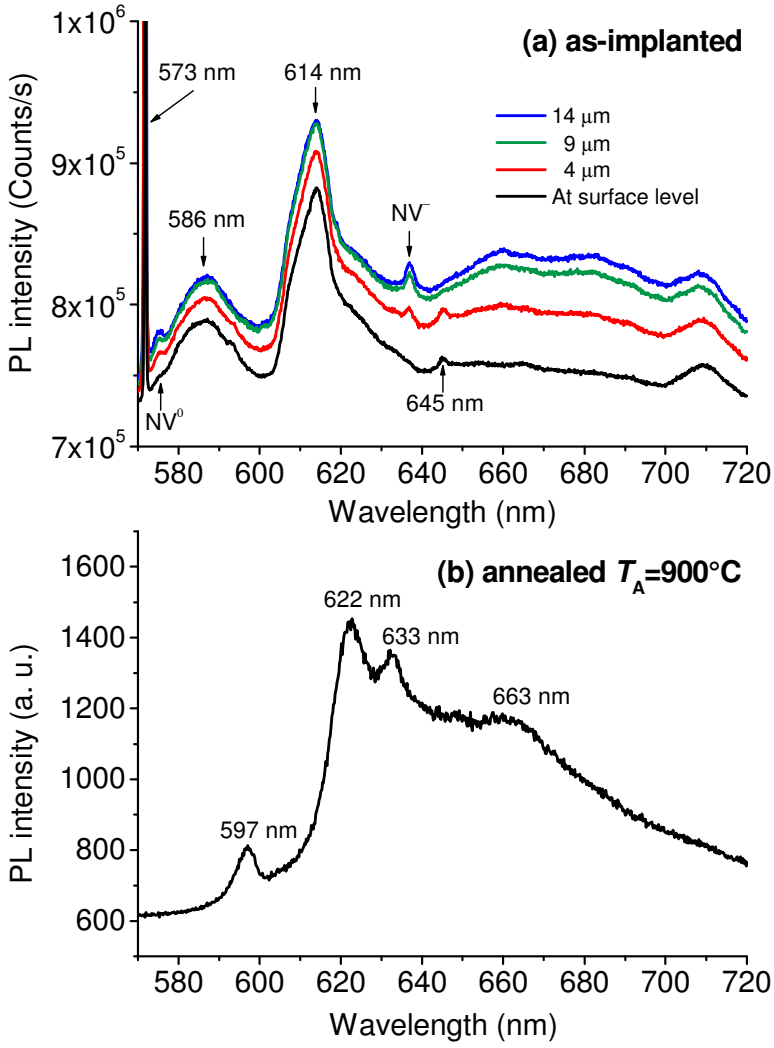

FIG. S13. PL spectra from the ^{120}Sn implanted backside of the sample, in the as-implanted state (a) and following annealing at 920°C (b). Note that the spectrum in the annealed state was measured only at surface level on a different setup (hence count rates are not comparable) and with a longpass filter reducing spectral response at shorter wavelengths.

fluence very reliable. While at ISOLDE the implantation currents for a beam that is collimated to 1 mm diameter on the sample are measured directly via the sample holder, which allows quite accurate determination of implantation fluences even in the 10^{12} cm^{-2} range, this was not possible with the Danfysik series 1090 high current implanter at KU Leuven. In order to keep the fluence low, the beam was swept by electrostatic deflection over a large area and its current density measured by four Faraday cups adjacent to the sample. This procedure can give wrong results for the fluence when there is a large fraction of neutral atoms present in the beam. The sample was measured with confocal PL in the as-implanted state as well as following 10 min vacuum annealing at 920°C (Fig. S13).

The PL spectrum in the as-implanted state [Fig. S13 (a)] shows, in addition to the first order Raman peak at 573 nm, broad lines around 586 and 614 nm. Since we have observed these features in diamond samples implanted with other elements, they are likely due to implantation damage. Focussing below the surface, the characteristic features of the NV^0 zero phonon line (ZPL) at 575 nm and the NV^- ZPL at 636 nm and associated phonon side bands at longer wavelengths are visible, reflecting the presence of nitrogen-associated defects in the natural IIa diamond.

After annealing at 920°C [Fig. S13 (b)], the wide peaks at 586 and 614 nm disappeared, and instead broad peaks around 597 nm, 622 nm, and 633 nm, as well as a broad shoulder around 663 nm are visible. The 622 nm peak represents the ZPL of SnV^-, while the structures at 633 nm and 663 nm are considered to be part of its phonon sidebands [13, 20]. Determining the FWHM of the 622 nm ZPL in this spectrum would require background correction, which could not be performed, however, it appears to be at least 8 nm. Overall this spectrum bears great similarity to what is reported in Fig. S1 of the supplemental material to Ref. [13], for CVD diamond samples implanted with 2×10^{13} atoms/cm^2 of ^{120}Sn and following annealing at 800°C. The broad peak around 595 nm was previously also interpreted as possibly Sn-related [12-13, 18].

Our best explanation for the difference in PL results found between the ^{121m}Sn+^{121m}Sn implantation at ISOLDE and the ^{120}Sn implantation at KU Leuven, is that in the latter case the fluence measurement was inaccurate and the effectively implanted fluence significantly higher than the targeted value.